remote sensing

MDPI

Article

A Study on Improved Langley Plot Calibration Methods Using Noise Reduction for Field Solar Spectral Irradiance (SSI) Observation Instruments

Guanrui Li [1,2], Aiming Zhou [3], Yu Huang [1,2,*], Xiaohu Yang [1,2] and Zhanfeng Li [1,2]

[1] Changchun Institute of Optics, Fine Mechanics and Physics, Chinese Academy of Sciences, Changchun 130033, China; liguanrui22@mails.ucas.ac.cn (G.L.); yangxiaohu@ciomp.ac.cn (X.Y.); lizhanfeng@ciomp.ac.cn (Z.L.)
[2] University of Chinese Academy of Sciences, Beijing 100049, China
[3] Shanghai Institute of Satellite Engineering, Shanghai 200240, China; lile09@mails.jlu.edu.cn
* Correspondence: huangyu@ciomp.ac.cn

Abstract: Accurate spectral and radiometric calibration is critical for precise Solar Spectral Irradiance (SSI) and Aerosol Optical Depth (AOD) retrievals in ground-based observations. This study introduces a pixel-based real-time noise deduction method and evaluates its performance using laser sources, Fraunhofer dark lines, and an improved Langley plot calibration. The proposed approach addresses challenges in long-term field SSI monitoring, including spectral noise variation and frequent calibration requirements for wavelength and responsivity corrections. The pixel-based noise deduction method effectively suppresses spectral dark noise to 0 ± 0.890, outperforming temperature-based corrections by 0.6%. Wavelength accuracy tests with laser sources and Fraunhofer dark lines demonstrate high consistency, with $\delta\lambda < 0.3$ nm, while spectral calibration uncertainty is assessed at 0.195 nm to 0.299 nm. The improved Langley plot achieves spectral responsivity differing by only 0.80% from the standard Langley plot and enhances AOD correlation with CE318 by 0.9–2.7% (RMSE: 0.002–0.003), significantly improving AOD observation accuracy. This work advances the development of field SSI hyperspectral observation and calibration, improving the accuracy of SSI and AOD measurements and contributing to the study of environmental changes and climate dynamics.

Keywords: Solar Spectral Irradiance (SSI); AOD; spectral calibration; Langley plot calibration; hyperspectral measurement

check for updates

Academic Editor: Manuel Antón

Received: 19 November 2024
Revised: 15 January 2025
Accepted: 22 January 2025
Published: 22 February 2025

Citation: Li, G.; Zhou, A.; Huang, Y.; Yang, X.; Li, Z. A Study on Improved Langley Plot Calibration Methods Using Noise Reduction for Field Solar Spectral Irradiance (SSI) Observation Instruments. *Remote Sens.* **2025**, *17*, 754. https://doi.org/10.3390/rs17050754

Copyright: © 2025 by the authors. Licensee MDPI, Basel, Switzerland. This article is an open access article distributed under the terms and conditions of the Creative Commons Attribution (CC BY) license (https://creativecommons.org/licenses/by/4.0/).

1. Introduction

Atmospheric constituents, including aerosol particles and gas molecules, play a pivotal role in shaping the atmospheric environment and influencing climate dynamics. Human activities, such as urbanization and industrial growth, have significantly altered the nature of atmospheric aerosols, leading to changes in their optical properties that impact the environment and drive climate change, both directly and indirectly [1–4]. Pollutant gases and aerosols generated by anthropogenic activities, such as sulfur dioxide (SO_2) and nitrogen oxides (NO_x), are gradually transformed into secondary particles, including sulfates and nitrates, within polluted atmospheres [5]. Studies have established that anthropogenic aerosols adversely affect air quality and pose serious health risks [6,7]. According to the Global Burden of Disease (GBD) study, exposure to fine particulate matter with aerodynamic diameters ≤ 2.5 μm (PM2.5) ranks as the sixth leading risk factor for human

disease, resulting in approximately 3.2 million premature deaths annually [8]. Beyond health implications, anthropogenic aerosol particles induce surface cooling by modifying surface temperatures and precipitation patterns. Furthermore, they disrupt the Earth's energy balance through the absorption and scattering of solar radiation, leading to negative radiative forcing attributable to human activities [9–13]. Conversely, greenhouse gases such as carbon dioxide (CO_2) emitted by anthropogenic sources contribute to positive radiative forcing, driving surface temperature increases and exacerbating global warming [14]. The dual impact of aerosols and greenhouse gases underscores the complexity of their interaction with the environment. Aerosols, in particular, present one of the greatest uncertainties in climate research, as their effects depend on critical parameters such as Aerosol Optical Depth (AOD), radius spectral distribution, and refractive index. AOD, defined as the integrated extinction coefficient of aerosols along a vertical atmospheric column, serves as a key indicator for assessing atmospheric turbidity and quantifying the degree of atmospheric pollution [15]. Due to the absorption and scattering optical properties of pollutant gases and aerosol particles in Solar Spectral Irradiance (SSI), SSI has become a crucial data source for investigating atmospheric phenomena. These studies rely on long-term, consistent SSI records. However, ground-based SSI measurement instruments are typically deployed in high-altitude field sites, where rapidly changing environmental conditions pose significant challenges to the long-term stability and accuracy of SSI records. As such, spectral and radiometric calibration of SSI instruments is indispensable, as it ensures the sustained accuracy of SSI data, thereby supporting scientific research into the effects of SSI on climate dynamics and atmospheric processes.

A sun photometer is an instrument designed to measure the intensity of SSI and serves as one of the primary ground-based remote sensing tools for deriving AOD. Instruments used for ground-based quantitative remote sensing of SSI are typically classified into channel-type and spectral-type sun photometers [15–19]. The calibration accuracy of these instruments is critical for ensuring reliable atmospheric remote sensing measurements. Over time, however, calibration values tend to drift due to prolonged operation and changes in environmental conditions, necessitating periodic spectral calibration and radiometric calibration [20,21].

Spectral calibration often involves the use of characteristic spectral line lamps or lasers to calibrate the wavelengths of spectral instruments, ensuring the precision of spectral wavelength measurements [22]. However, the signal-to-noise ratio (SNR) of characteristic spectral line lamp signals in SSI observation instruments is relatively low, making laboratory-based calibration using high-energy tunable lasers a more practical approach. For long-term stationary SSI observations in the field, transporting instruments to a laboratory for recalibration can be prohibitively expensive. Fortunately, the Sun's rich Fraunhofer line spectrum provides an opportunity for on-site spectral calibration of SSI observation instruments [23].

Radiometric calibration of SSI instruments primarily employs the contrast transfer method, the standard light source method, and the Langley plot calibration method [24–27]. The contrast transfer method is well-suited for channel-type sun photometers, while Langley plot calibration is more appropriate for field calibration of spectral-type sun photometers compared to the standard light source method. However, the Langley plot technique imposes stringent requirements on the stability of AOD and atmospheric turbidity during calibration. Given the variability of atmospheric conditions across calibration days, Langley plot calibration values are typically averaged over monthly or weekly intervals to improve reliability.

Since the accuracy of spectral and radiometric calibrations directly influences the observational precision of SSI measurements, laboratory-based calibrations are not always

practical in certain scenarios. To address this limitation and enhance on-site spectral and radiometric calibration methods for SSI observation instruments, this study explores two key approaches. First, the wavelength accuracy of the instruments is validated by comparing the spectral calibration results obtained using instrument lasers with the Fraunhofer line observations of SSI. Second, the feasibility of an improved Langley plot method is examined by refining the traditional Langley plot technique and comparing its results with the AOD retrieval outcomes from the CE318 sun photometer. These comparisons demonstrate the potential of the proposed methods to improve the calibration accuracy for field-based SSI observations.

2. Data Sources and Calibration Theory

2.1. Data Sources

The SSI observation instrument used in this study is the Ground Solar Spectral Irradiance Monitor (GSSIM), developed by the Changchun Institute of Optics, Fine Mechanics, and Physics (CIOMP). Unlike SSI observation instruments based on filter wheel structures, GSSIM provides full-spectrum, high-resolution observations of the Sun. GSSIM includes a hyperspectral measurement unit, a solar tracking turntable, and auxiliary units featuring a modular design for easy component replacement and enabling automated all-day SSI measurements. The hyperspectral detection unit uses an optical fiber spectrometer with an Ultra-low Stray Light (ULS) symmetrical Czerny–Turner design, optimizing the arrangement and materials of the optical components (grating, mirrors, and lenses) to minimize stray light.

During solar tracking and observation, SSI is coupled into the spectrometer slit via an optical fiber, passes through a collimation optical path, and is dispersed by a grating. Although longer optical fibers may cause more signal loss, increasing the integration time can ensure an adequate signal. The dispersed light is focused onto a linear Charge-Coupled Device (CCD) array detector by a focusing mirror. The detector features a thin, back-illuminated CCD image sensor with a 1588 $\times$ 1 $\times$ 64 pixel array. The 1588 pixels are arranged horizontally on the focal plane, while 64 pixels are stacked vertically. Each pixel measures 14 μm $\times$ 14 μm, with a height of 0.89 mm. This stacking design increases the photosensitive area on the focal plane, improving the sensitivity of spectral measurements. The thin structure of the detector also provides excellent thermal inertia and conductivity, allowing for rapid thermal equilibrium and minimizing temperature gradients. The CCD converts the light signal into a voltage signal, which is subsequently digitized into dimensionless digital signals. The solar tracking turntable features a T-shaped structure, optimizing the instrument's lightweight tracking design, and employs a dual algorithm for tracking, combining computational tracking and four-quadrant detector tracking. This system achieves a tracking accuracy better than 0.08°. The auxiliary unit includes a temperature control system and a microcomputer. The temperature control system mitigates spectral noise and wavelength drift, while the microcomputer supports the automated observation program, which starts data collection when the solar altitude angle exceeds 0°. Together, these units enable unattended outdoor SSI observations. Table 1 summarizes key design specifications and performance characteristics of GSSIM.

In this study, the spectral test site for the GSSIM is located at the Changchun Institute of Optics, Fine Mechanics, and Physics, situated in Erdao District, Changchun City, Jilin Province, with coordinates of 43°51′46.8″N, 125°22′11.3″E, and an average altitude of 200 m. The radiometric calibration and SSI observation site is located at the Twin Astronomical Observatory in Gaomei Gucun, Yulong County, Lijiang City, Yunnan Province, with coordinates of 26°43′21″N, 100°01′46″E, and an altitude of 3170 m. The operational status of the instruments at both Changchun and Lijiang sites is illustrated in Figure 1. Compared

to Changchun, the Lijiang site offers superior astronomical observation conditions, including low latitude, high altitude, weak atmospheric extinction, and excellent atmospheric stability, making it highly suitable for SSI calibration and observation [28]. For this study, data for the Langley plot calibration were selected from March 2024 observations at the Lijiang site, which experienced a higher proportion of clear-sky days, providing optimal conditions for radiometric calibration.

Meanwhile, a fully automated CE318 sun photometer, manufactured by CIMEL in France and subjected to rigorous radiometric calibration, was deployed near the GSSIM. This instrument was used to measure SSI in discrete spectral bands and to retrieve atmospheric parameters such as AOD [29]. In the subsequent discussion of this paper, the CE318 is used as a reference standard instrument to evaluate the calibration accuracy and retrieval results of the GSSIM.

Table 1. Selected Spectral Performance Parameters of GSSIM.

Performance Parameter	Value
Spectral Wavelength Range	285 nm~1000 nm
Spectral Resolution	<2.5 nm
Spectral Spacing	0.6 nm
Wavelength Accuracy	±0.3 nm
Wavelength Repeatability	±0.05 nm



(**a**) (**b**)

Figure 1. On-site images of GSSIM at Changchun and Lijiang. (**a**) Changchun; (**b**) Lijiang.

2.2. Spectral and Radiometric Calibration Theory

2.2.1. Spectral Calibration and Spectral Testing

The accuracy of fine spectral analysis of solar radiation and the retrieval of atmospheric optical properties, such as AOD, is highly dependent on the precise calibration of observing instruments. Spectral calibration and testing in the laboratory are essential steps to verify whether the instrument meets design specifications before radiometric calibration and outdoor deployment. The spectral calibration process utilizes a tunable laser to identify the CCD pixel numbers corresponding to multiple characteristic wavelengths. A polynomial fit is then applied to establish the relationship between the wavelength and the CCD pixel number across the full spectral range. Once the pixel center wavelengths are determined, comprehensive spectral testing is conducted. This includes evaluating key parameters

such as spectral range, spectral spacing, spectral resolution, wavelength accuracy, and wavelength repeatability.

$$f(\lambda) = \mathrm{a} \cdot \mathrm{e}^{(\,-(\lambda\,-\,\lambda_c)^2/\,2\sigma^2)}, \tag{1}$$

During laboratory spectral testing, a tunable laser emits monochromatic light at specified wavelengths (λ) to irradiate the instrument's pupil. The response signal values per unit integration time at different wavelengths are recorded for the target pixel over n repeated measurements. These measurements are fitted and normalized using the spectral response function $f(\lambda)$, as described by Equation (1). The resulting spectral response function is illustrated in Figure 2. Here, a represents the normalized amplitude, λ_c is the central wavelength, and σ denotes the standard deviation. The spectral spacing $\Delta\lambda_i$ is expressed as $\Delta\lambda_i = |\lambda_{i+1} - \lambda_i|$, which is the absolute difference between the central wavelengths of adjacent pixels. The spectral resolution $d\lambda_i$ reflects the instrument's ability to distinguish different wavelengths within a given range, and its value is the full-width at half-maximum (FWHM) of $f(\lambda)$.

$$\mathrm{U} = \sqrt{\mathrm{U}_1^2 + \mathrm{U}_2^2 + \mathrm{U}_3^2 + \cdots + \mathrm{U}_m^2}, \tag{2}$$

Wavelength accuracy δλ characterizes the precision of the instrument's measurement of a specific wavelength, defined as the deviation between the measured wavelength λ_a and the true wavelength λ_t. Typically, the output wavelength of the tunable laser is taken as the true wavelength λ_t, while λ_a represents the average value of multiple measurements of λ_c. Wavelength repeatability s describes the instrument's capability to maintain consistent wavelength measurements over repeated tests. It is defined as the standard deviation of the central wavelength λ_c across multiple measurements, reflecting the instrument's wavelength stability during long-term operations.

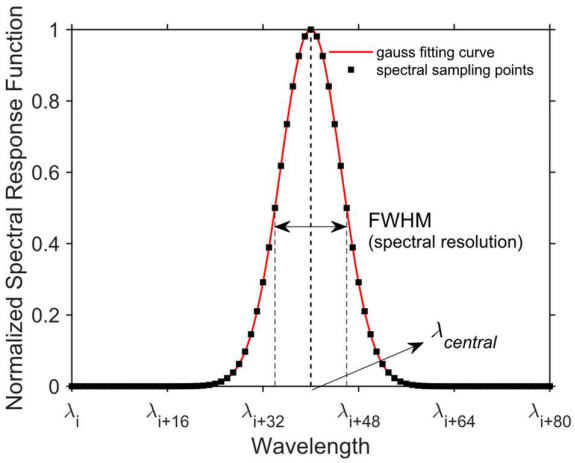


Figure 2. Schematic Diagram of the Normalized Spectral Response Function.

Table 2 summarizes the formulas for calculating key spectral performance parameters during spectral testing. To quantify the accuracy of the instrument's spectral calibration, we employ a Type B uncertainty evaluation. The uncertainty synthesis formula is provided in Equation (2).

Table 2. Formulas for Calculating Spectral Performance Parameters of GSSIM.

Performance Parameter	Value
Spectral Wavelength Range	$[\lambda_{\min} \sim \lambda_{\max}]$
Spectral Resolution ($d\lambda_i$)	$d\lambda_i = \mathrm{FWHM} = 2\sqrt{2\ln 2}\cdot\sigma$
Spectral Spacing ($\Delta\lambda_i$)	$\Delta\lambda_i = \lambda_{i+1} - \lambda_i$
Wavelength Average Value (λ_a)	$\lambda_a = \frac{1}{n}\sum_{i}^{n}\lambda_c(i)$
Wavelength Accuracy ($\delta\lambda$)	$\delta\lambda = \mid \lambda_a - \lambda_t \mid$
Wavelength Repeatability (s)	$s = \sqrt{\frac{1}{n-1}\sum_{i}^{n}(\lambda_a - \lambda_c(i))^2}$

2.2.2. Radiometric Calibration

To quantify the consistency and accuracy of the instrument's measurements with the true physical quantities, it is necessary to evaluate the measurement repeatability, SNR, and spectral responsivity of the instrument.

Measurement repeatability δ_m assesses the stability and reliability of the instrument's measurements. It is evaluated using the coefficient of variation of the daily continuous measurement data. The SNR is used to evaluate the quality of the signal, representing the ratio of signal strength to background noise. A higher SNR indicates better instrument performance. Spectral responsivity K(λ) establishes a relationship between the digital number (DN) output of the GSSIM and the true SSI value. The spectral responsivity of the instrument per unit integration time is defined as:

$$E(\lambda) = V(\lambda)/K(\lambda), \quad (3)$$

where E(λ) represents the true SSI value, and V(λ) is the instrument's response signal value DN under this irradiance. The unit of K(λ) is unit $(W\ m^{-2}\ nm^{-1})^{-1}$.

Because the extinction effects of aerosols and clouds on solar radiation vary significantly from day to day, while solar irradiance at the top of the atmosphere (TOA) remains nearly constant, the radiometric calibration of GSSIM focuses on establishing the relationship between SSI and DN at the TOA. Bouguer's law, in combination with Equation (3), can be rewritten as:

$$\ln\left[V(\lambda)R^2\right] = \ln[V_0(\lambda)] - m\tau(\lambda), \quad (4)$$

where V(λ) is the DN at each wavelength obtained from ground-based measurements, R^2 is the Sun–Earth distance correction factor, V_0 is the equivalent measured DN value at the TOA, m is the air mass (AM), and τ(λ) is the AOD. The correction factor R^2 is calculated as:

$$R^2 = \left(d/d_0\right)^2, \quad (5)$$

where d is the actual Sun–Earth distance on the day of observation, and d_0 is the mean Sun–Earth distance. In Equation (4), a first-order linear relationship is established by plotting m as the x-axis and $\ln[V(\lambda)R^2]$ as the y-axis. The straight-line intercept b corresponds to the calibrated value of $V_0(\lambda)$, which is then used in Equation (3) to derive the responsivity K(λ). This forms the basis of the Langley plot on-site calibration for SSI observations.

To avoid the influence of gas absorption bands on K(λ) after accounting for the extinction caused by absorbing gases, the $V_0(\lambda)$ values within the gas absorption bands are obtained by linearly interpolating the $V_0(\lambda)$ values from adjacent non-absorption bands. The responsivity K(λ) for the gas absorption bands is then calculated accordingly. Xiaoxiao Tang compared the calibration results of this method with those of a standard instrument andonfirmed its consistency [30]. This method is therefore adopted in this study for the

interpolation process. Table 3 provides the formulae for key radiometric properties used in the radiometric calibration, and the uncertainty of the radiometric calibration is calculated using Equation (2). Figure 3 illustrates the entire calibration process of GSSIM in the field.

Table 3. Formulas for Calculating Selected Radiometric Performance Parameters of GSSIM.

Performance Parameter	Value
Average Value of n-Time Measured Signals $V_a(\lambda)$	$V_a(\lambda) = \frac{1}{n}\sum_i^n V(\lambda).$
Standard Deviion of n-Time Measured Signals $s_V(\lambda)$	$s_V(\lambda) = \sqrt{\frac{1}{n-1}\sum_i^n (V(\lambda) - V_a(\lambda))^2}$
Measur.ment Repeatability $\delta_m(\lambda)$	$\delta_m(\lambda) = \frac{s_V(\lambda)}{V_a(\lambda)}$
Signal-to-Noise Ratio SNR(λ)	$SNR(\lambda) = \frac{V_a(\lambda)}{s_V(\lambda)}$
Spectral Responsivity K(λ)	$K(\lambda) = V(\lambda)/E(\lambda)$

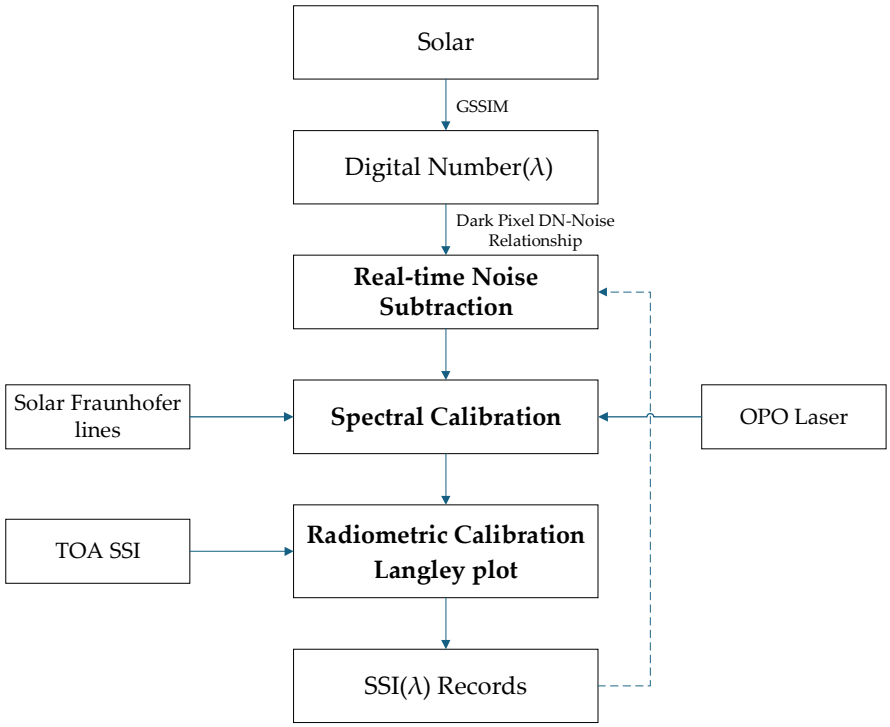


Figure 3. Flowchart of Spectral and Radiometric Calibration for SSI.

3. Testing and Calibration

3.1. Two Methods for Handling Solar Spectral Dark Noise

The spectral noise of the spectrometer must be analyzed and subtracted before the instrument undergoes testing and calibration, as the presence of noise directly affects the accuracy and repeatability of SSI observations. Analysis reveals that the primary component of spectral noise is dark noise, which arises from electron-hole pairs generated by the CCD detector at varying temperatures. This dark noise contributes to the DN statistics of each image element, making it highly correlated with temperature. Therefore, the noise in field SSI observations exhibits a significant dependence on environmental temperature, which poses a challenge to the stability of long-term SSI records.

To address this issue, the GSSIM incorporates a temperature control module during its design and manufacturing to suppress spectral noise. However, the internal detector's temperature still fluctuates to some extent and it is challenging to monitor precisely in

practice. As a result, it is necessary to dynamically subtract real-time dark noise from the instrument's measurements to ensure accurate results. Noise reduction methods for ground-based SSI instruments are mainly divided into physical and algorithmic approaches. Physical methods use mechanical structures for light shielding, which leads to complex designs and slower measurement speeds. Algorithmic methods suppress dark noise by monitoring instrument states, but inaccuracies in measurements or models can introduce new noise. To address this, we propose a pixel-based noise reduction method that enables real-time noise reduction without relying on mechanical structures or external measurements.

Due to the extinction of solar radiation by the Earth's atmosphere, SSI below 300 nm is negligible when it reaches the surface. Therefore, the DN output from the instrument in the wavelength range below 300 nm can be regarded as spectral dark noise, which is solely influenced by temperature. As described in the Data Sources section, the spectrometer uses a symmetrical Czerny–Turner optical design and a thin CCD detector. This ensures uniform heat distribution for rapid thermal equilibrium. A temperature control system protects the instrument from external temperature fluctuations, preventing uneven pixel temperature. Based on these conditions, we assume the internal temperature affects all pixels uniformly.

Consequently, the dark noise of pixels with center wavelengths below 300 nm (referred to as dark pixels) should be highly correlated with that of the remaining pixels. In SSI measurements, the DN values of dark pixels represent pure dark noise, while the DN values of the remaining pixels contain both dark noise and the effective optical signal. By using the DN values of dark pixels to estimate the dark noise of other pixels, it becomes possible to calculate and subtract the dark noise from the remaining pixels in real time. This method provides a practical approach for real-time dark noise deduction in the instrument.

We masked the instrument's incident pupil and conducted measurements every minute for a total of 8 h (480 measurements) to obtain the spectral dark noise per unit integration time. During the measurements, we also recorded the temperature changes of the internal instrument and the inner surface of the spectrometer. The scatter plot of the dark noise versus temperature for the 500th pixel is shown in Figure 4a. The 500th pixel on the spectrometer's focal plane, selected from top to bottom, is presented due to its spectral response center wavelength being approximately 570 nm, where the SSI's DN value is relatively high, providing the maximum signal-to-noise ratio, which is of particular interest in our analysis. The gray triangular scatter points in the figure represent the dark noise as a function of the control box temperature ($temperature_{inbox}$), while the black circular scatter points represent the dark noise as a function of the spectrometer temperature ($temperature_{spectrometer}$). In the design of GSSIM, the spectrometer is fixed inside the box for temperature control, meaning that the $temperature_{inbox}$ reflects the ambient temperature of the spectrometer, while the $temperature_{spectrometer}$ is considered to be the temperature of the detector. It is evident that the black scatter points are shifted approximately 1.5 °C to the right compared to the gray scatter points. This shift is due to the heat generated by the spectrometer during operation, resulting in a higher $temperature_{spectrometer}$ than the $temperature_{inbox}$ once thermal equilibrium is reached. Polynomial fitting between $temperature_{spectrometer}$ and pixel dark noise shows that a second-order polynomial provides a better fit than a first-order polynomial, with a correlation coefficient of $r = 0.9964$, indicating a high degree of correlation. Therefore, using temperature to deduct dark noise is a feasible approach. Figure 4b illustrates the correlation between the DN values of the 500th, 750th, 1000th, and 1250th pixels and those of the dark pixels. The pixels exhibit extremely high linear correlations, with $r = 0.9976 \sim 0.9979$. This method shows a slightly higher correlation than that in Figure 4a. The model adopts a simple first-order linear relationship, ensuring consistent environmental influence across pixels and avoiding new

uncertainties introduced by temperature measurements. Thus, this work employs the model described in Equation (6) to achieve real-time spectral dark noise deduction at the pixel level.

$$V(\lambda) = I(\lambda) - N(\lambda) = I(\lambda) - (k(\lambda) \cdot N_0 + b(\lambda)), \quad (6)$$

where V(λ) is the effective DN value of the pixel, I(λ) is the DN value output by the pixel, N(λ) is the simulated dark noise of the pixel, and N_0 is the DN value of the dark pixel. k(λ) and b(λ) are the parameters of the fitted first-order polynomial. For comparison, we also provide a noise reduction model (Equation (7)) that uses the spectrometer temperature T as the independent variable. In this model, a, b, and c are the coefficients of the fitted second-order polynomial:

$$V(\lambda) = I(\lambda) - N(\lambda) = I(\lambda) - (a(\lambda) \cdot T^2 + b(\lambda) \cdot T + c(\lambda)), \quad (7)$$

In Figure 5a–c, we show the variation in dark noise across all pixels throughout the day under field conditions. These three figures are 2-D plots, which illustrate the variation in dark noise before and after denoising across two dimensions: the spectral dimension (1-D) and the temporal dimension (1-D). Indexing along the x-axis represents the variation in the same pixel over the course of the entire day, while indexing along the y-axis shows the change in dark noise with respect to wavelength at the same time point. The results are presented for three cases: untreated dark noise, dark noise corrected using the temperature-based model (Equation (7)), and dark noise corrected using the dark pixel DN values (Equation (6)). Without noise correction, the temperature control unit inside the instrument, which operates in periodic heating and cooling cycles, causes the dark noise to fluctuate within a small range throughout the day. The overall daily variation for all pixels is 134.0 ± 1.32670 ($k_{0.95}$ = 1.96). After applying the two noise reduction methods, the dark noise across all pixels becomes nearly constant over time, indicating that the influence of internal temperature fluctuations on dark noise is significantly reduced. This stabilization is beneficial for maintaining the temporal stability of spectral noise during all-day observations.

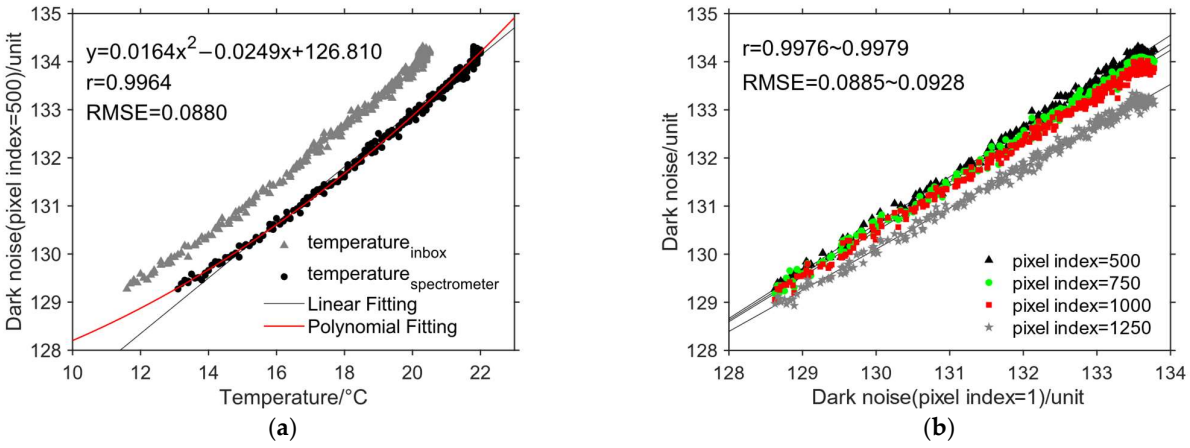


Figure 4. (**a**) Nonlinear relationship between the internal temperature of the instrument and the dark noise of the 500th pixel; (**b**) Correlation scatter plot of dark noise between dark pixels and other pixels (>300 nm).

In Figure 5c, the uniformity of pixel dark noise is better than in Figure 5b. The temperature-based noise correction method shows larger fluctuations in the dark noise around 800 nm and 950 nm. These deviations result from inconsistencies between pixel dark noise and temperature measurements due to factors such as temperature measure-

ment accuracy, cooling location, and pixel manufacturing variations, leading to poorer model fitting for certain pixels and higher noise levels. Figure 6a presents the standard deviation of daily dark noise variations across all pixels after applying the two correction methods. The dark pixel DN value method achieves overall lower variation compared to the temperature-based method. The overall noise levels are 0 ± 0.8870 ($k_{0.95} = 1.96$) and 0 ± 0.8980 ($k_{0.95} = 1.96$), respectively, showing a 1.2% improvement in performance with our proposed method. Figure 6b displays the histograms of dark noise distributions for the two correction methods. Assuming a normal distribution of dark noise, the dark noise corrected using the dark pixel DN value method exhibits a more concentrated distribution (dark $noise_{dark\ pixel} = 0 \pm 0.899$ ($k_{0.95} = 1.96$), dark $noise_{temperature} = 0 \pm 0.960$ ($k_{0.95} = 1.96$)). This is consistent with the results shown in Figure 6a.

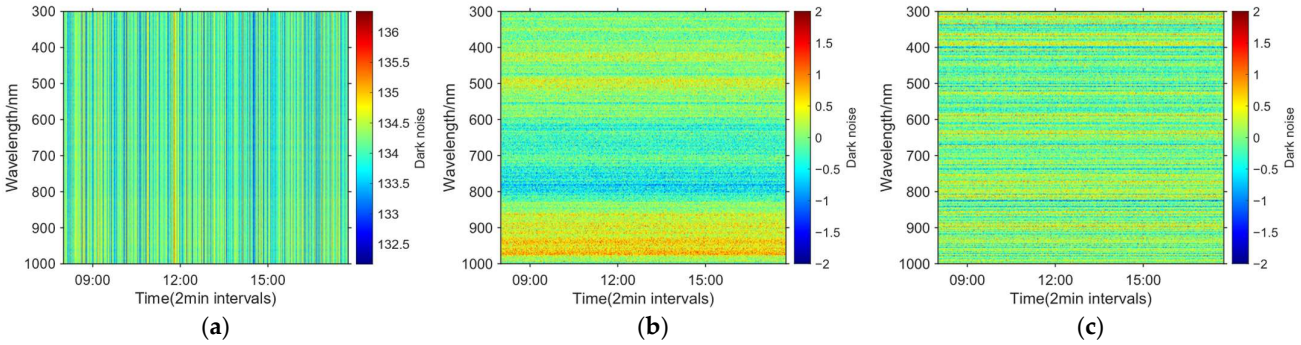


Figure 5. 2-D Distribution of Spectral Dark Noise in the Spectrometer (x: 1-D Temporal Dimension, y: 1-D Spectral Dimension). (**a**) Untreated; (**b**) Using temperature as the independent variable; (**c**) Using the dark pixel DN value as the independent variable.

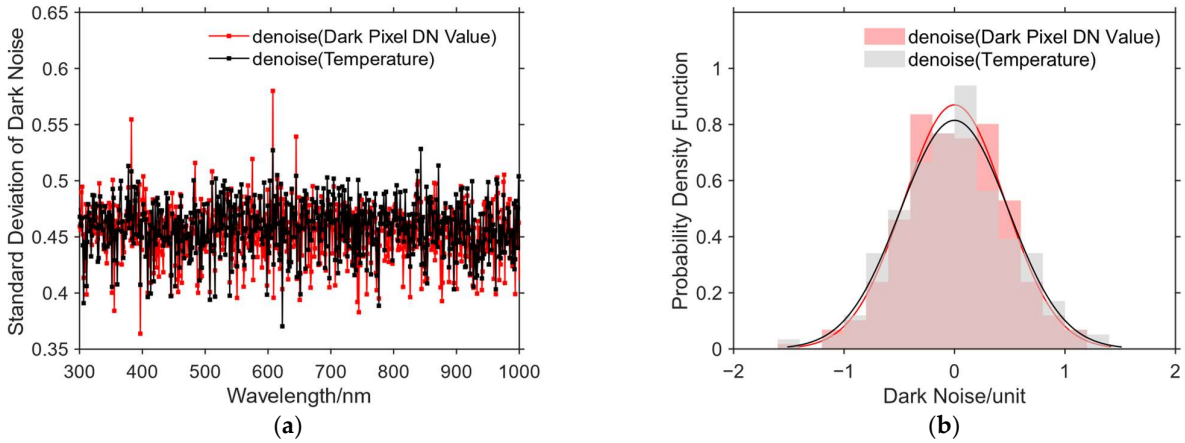


Figure 6. (**a**) Daily standard deviation of dark noise across all pixels after applying the two noise reduction methods; (**b**) Probability distribution histograms of dark noise for the 500th pixel after applying the two noise reduction methods.

The dark pixel-based noise reduction method effectively suppresses spectral noise and outperforms temperature-based methods. It addresses the low measurement speed and potential mechanical failure issues associated with physical noise reduction techniques, making it suitable for the harsh conditions of field SSI observations. Compared to temperature-based methods, this approach does not rely on internal instrument state measurements, making it more universally applicable to commercial spectrometers. This enhances the modular assembly of SSI observation instruments, reducing both observation and maintenance costs.

3.2. Spectral and Radiometric Testing

3.2.1. Spectral Testing

After applying noise reduction to the GSSIM, spectral testing was conducted in December 2023 in Changchun to evaluate its spectral performance. In a standard laboratory setting, a calibrated EKSPLA NT242 Optical Parametric Oscillator (OPO) laser, manufactured by EKSPLA and located in Vilnius, Lithuania, was used as the monochromatic light source instead of a characteristic spectral line lamp. The OPO laser was selected because it can emit pulses with significantly higher power compared to the characteristic spectral line lamp (e.g., the AvaLight-CAL-Mini emits approximately 1.6 μW). This higher power enables the spectrometer to complete measurements without requiring long integration times. Table 4 lists some key parameters of the Ekspla NT242 OPO laser. Regarding the wavelength accuracy of the laser, Christopher W. Stubbs et al. compared it with Hg–Ar line lamp (Ocean Optics HG-1) and demonstrated that the Ekspla NT242 OPO achieves a wavelength accuracy of approximately σ_λ~0.2 nm [31].

Table 4. Selected Performance Parameters of the EKSPLA NT242 OPO Laser.

Performance Parameter	Value
Tunable Wavelength Range	285 nm~2300 nm
Pulse Energy (OPO)	450 μJ
Pulse Duration	3~6 ns
Wavelength Accuracy	0.2 nm

After preheating the NT242 OPO laser for 5 h, the instrument was controlled to continuously collect five frames of output monochromatic light. The spectral response function $f(\lambda)$ was derived by fitting the spectral sampling points using Equation (1). Due to space limitations, only the results for 400 nm and 700 nm are presented in Figures 7 and 8.

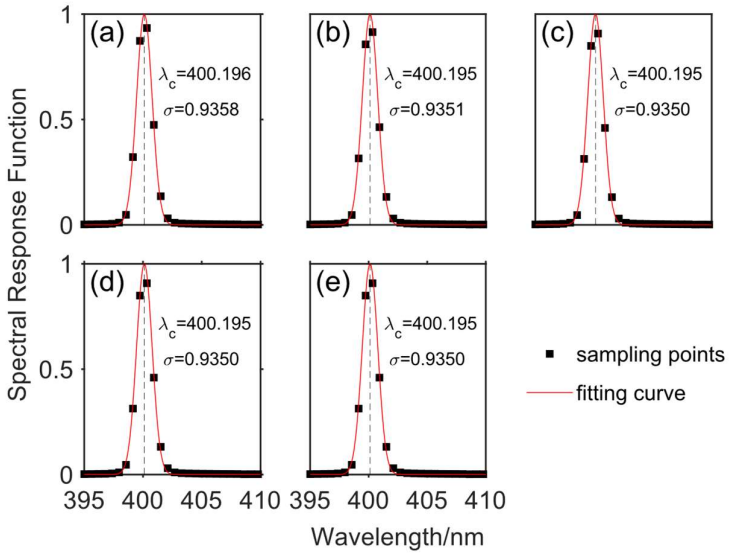


Figure 7. Spectral Response Function for an Incident Wavelength of 400 nm. (**a**) First Measurement; (**b**) Second Measurement; (**c**) Third Measurement; (**d**) Fourth Measurement; (**e**) Fifth Measurement.

The fitted wavelengths λ_a were 400.195 ± 0.00051 (k = 1) and 700.223 ± 0.0028 nm (k = 1), respectively. The instrument's wavelength accuracy δλ was 0.195 nm (400 nm) and 0.223 nm (700 nm). Wavelength repeatability s was 0.00051 nm (400 nm) and 0.0028 nm (700 nm). The spectral resolution (FWHM) was 2.202 nm (400 nm) and 2.212 nm (700 nm), meeting the technical specifications of the instrument design.

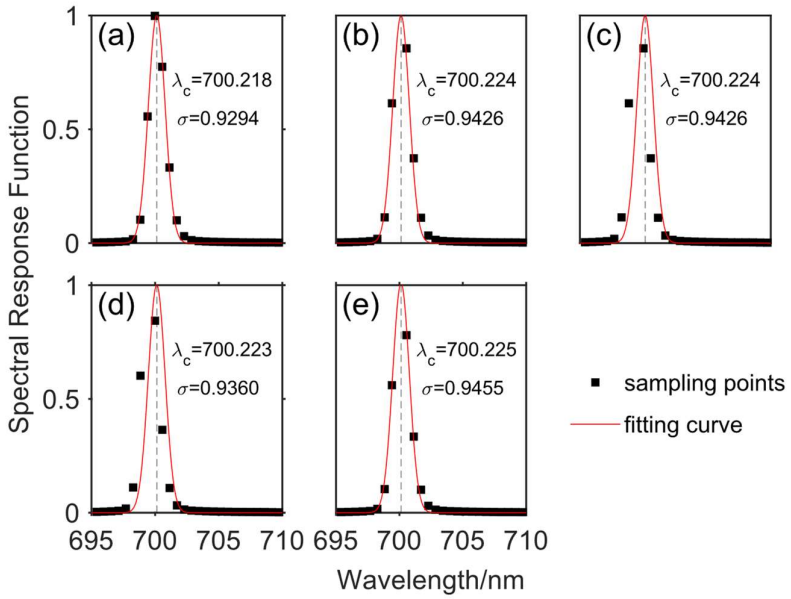


Figure 8. Spectral Response Function for an Incident Wavelength of 700 nm. (**a**) First Measurement; (**b**) Second Measurement; (**c**) Third Measurement; (**d**) Fourth Measurement; (**e**) Fifth Measurement.

3.2.2. Radiometric Calibration

The radiometric testing of GSSIM used the midday Sun under clear weather conditions as the standard light source. Through multiple short-duration measurements (t < 10 s) of SSI, the measurement repeatability δ_m and signal-to-noise ratio (SNR) were determined using the formulas provided in Table 3. The testing was conducted outdoors in Changchun during the winter of December 2023, as shown in Figures 1a and 9a,b, which present the instrument's measurement repeatability δ_m and SNR. It is evident that δ_m deteriorates sharply below 300 nm. This is attributed to the near-zero SSI reaching the surface in this wavelength range, causing the degradation in δ_m to be primarily driven by spectral dark noise. This also explains the near-zero SNR observed below 300 nm in Figure 9b. In non-gas absorption bands, δ_m fluctuates around 0.226% overall. However, due to the reduced light flux received by the spectrometer's edge pixels, δ_m exhibits the largest degradation, up to 6.12%, in the 300 nm to 450 nm range. In gas absorption bands, δ_m deteriorates to 0.229% (O_2) and 0.342% (H_2O). Simultaneously, Figure 9b shows that the SNR decreases to 226 and 176 in these bands, respectively. This reduction is caused by the extinction of SSI by absorbing gases, which lowers the DN values measured by the ground-based instrument.

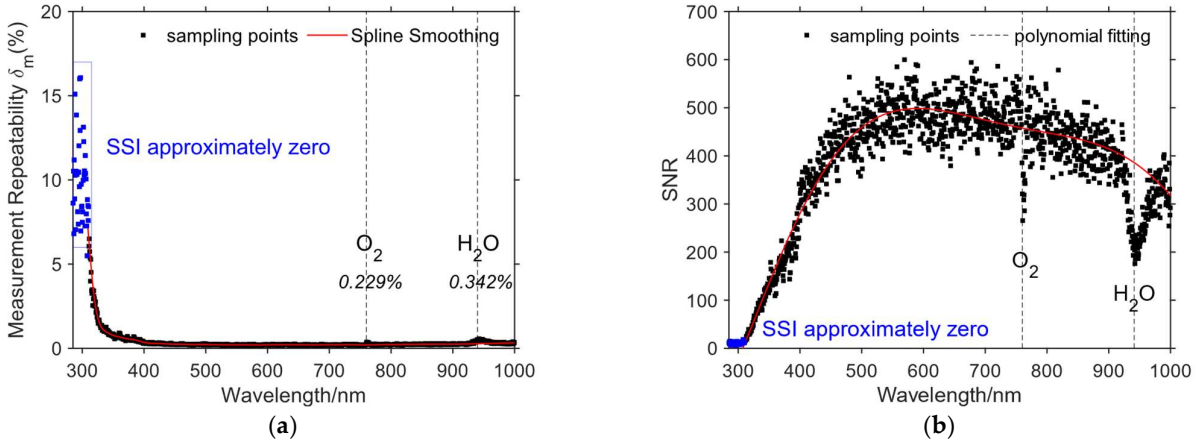


Figure 9. Radiometric Testing and Calibration Results Within the Spectral Range of the Instrument. (**a**) Measurement Repeatability; (**b**) Signal-to-Noise Ratio (SNR).

To ensure the long-term accuracy of the instrument's observations, regular radiometric calibration is required to account for changes in the field environment (such as window glass attenuation, optical fiber aging, etc.). The field-based Langley plot calibration method does not rely on laboratory light sources but instead traces the reference source back to the Sun, providing a solution to address the challenges of maintaining the accuracy of SSI long-term records. After completing the radiometric performance testing of the instrument, Langley plot field calibration was conducted to determine the spectral responsivity K(λ) of the instrument. The daily variation in SSI DN values at 550 nm and 936 nm is shown in Figure 10a,b. At 550 nm, the curve is sparser on the left side due to larger variations in air mass (m). The SSI DN curves for the five selected calibration mornings exhibit smooth and continuous characteristics, although differences in trends are observed due to varying measurement conditions, such as solar zenith angle, aerosols, and clouds on different days. At 936 nm, located in the water absorption band, the extinction of SSI by atmospheric column water vapor causes a reduction in SNR. Consequently, the curves over the five days show some degree of fluctuation and offset compared to those at 550 nm. Figure 10c presents the full-spectral-range DN variation throughout day 2. The DN values remain smooth over the entire day, clearly illustrating the variation patterns of SSI.

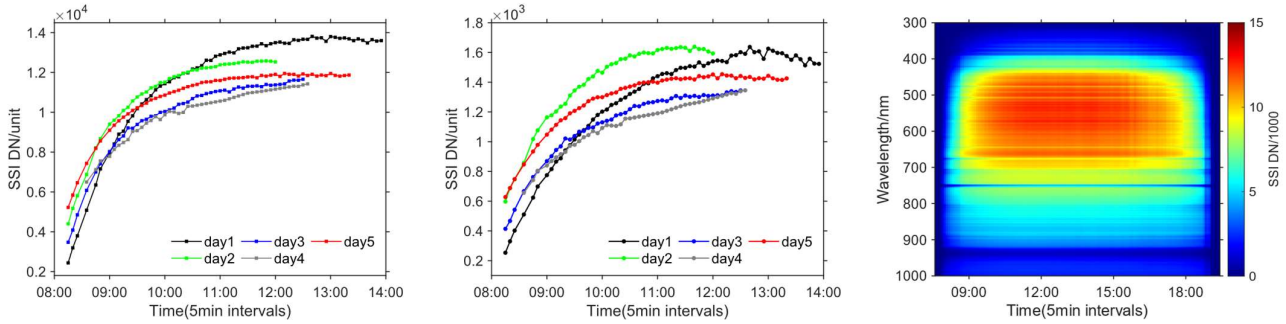


Figure 10. GSSIM SSI DN Values in Lijiang (March). (**a**) 550 nm; (**b**) 936 nm; (**c**) Day 2 DN Variation Across the Full Spectral Range During Daytime.

By extrapolating the linear relationship $\ln[V(\lambda)R^2] - m$, $V_0(\lambda)$ was obtained. Figure 11a illustrates the Langley plot linear relationship at 550 nm. In the figure, two methods are employed: (a) the averaged Langley plot, where five calibration dates are fitted separately using Equations (3) and (4) to obtain $V_0(\lambda)$ and K(λ). The arithmetic mean of the spectral responsivities K(λ) from the five calibration days is then calculated, and this average K(λ) is used as the spectral responsivity obtained by the averaged Langley plot method. (b) the integrated Langley plot, where the five calibration days are treated as a single dataset. The DN values of the SSI observed over the five days and the air quality m are integrated into a single column of DN and a single column of m. The spectral responsivity for the entire five-day period is then calculated using Equations (3) and (4). This approach was designed to compare the impact of the two methods on the determination of K(λ) and their subsequent effects on AOD retrieval results. The results of linear regression are represented by colored solid lines for individual days and a black solid line for the combined data. The intercept corresponds to the calibration value $V_0(\lambda)$, while the slope indicates the average variation in AOD during the Langley plot period. The correlation coefficient r of the linear regression indirectly evaluates the stability of AOD changes on calibration days. For the five calibration days, r values were all greater than or equal to 0.991, except for day 5, where r dropped to 0.981 near 760 nm (O_2). This indicates that the selected calibration days had relatively stable aerosol extinction, providing an ideal environment for Langley plot field calibration.

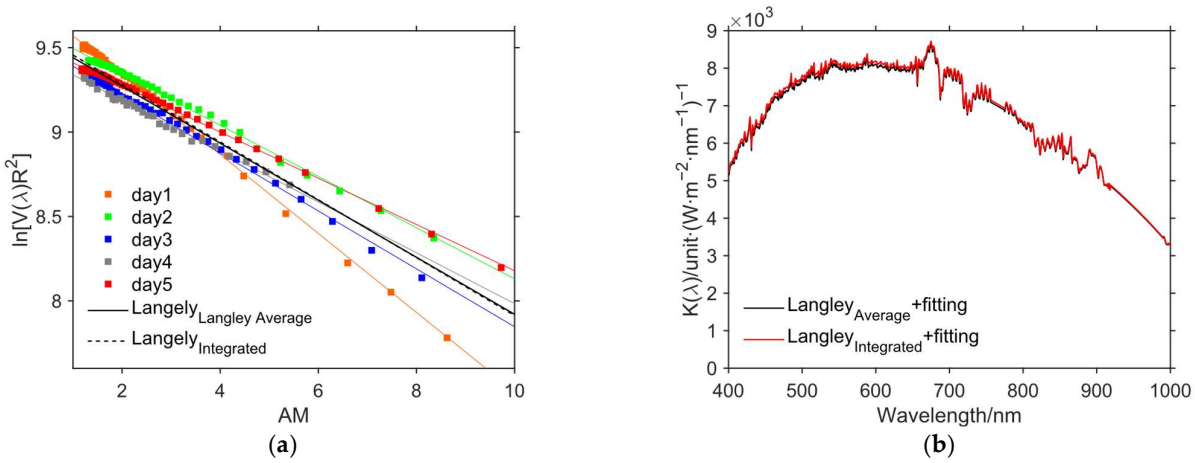


Figure 11. (**a**) Langley plot relationships for the five calibration days; (**b**) Interpolation-corrected spectral responsivity of GSSIM.

Subsequently, the finely resolved SSI observed by the FY-3E payload SSIM was convolved with the slit function of GSSIM and sampled at the same wavelength intervals. Compared to similar space-based SSI observation payloads, the GSSIM offers higher spectral resolution, particularly in the ultraviolet wavelength range. Due to the ease of data acquisition, we use the GSSIM to obtain spatial SSI values. The convolution result was used as $E_0(\lambda)$, and the average K(λ) from the five calibration days and the K(λ) from the integrated Langley plot were calculated. As shown in Figure 11b by the black and red curves, the interpolation-corrected K(λ) values obtained from the two Langley plot methods differ by 0.78% across the entire spectral range and by 0.51% in gas absorption bands. The consistency of K(λ) between the two methods demonstrates their reliability.

3.3. Uncertainty Assessment

The uncertainty assessment for spectral and radiometric calibration is primarily based on partial measurement data and calibration certificates, employing the Type B evaluation method. This study focuses on the relative radiometric calibration accuracy, spectral calibration uncertainty, and absolute radiometric calibration uncertainty.

In the continuous solar measurement mode, the relative radiometric calibration accuracy is mainly influenced by the instrument's measurement repeatability, solar tracking accuracy, atmospheric inhomogeneity, and solar radiation stability. According to calculations, the measurement repeatability of the instrument is 0.226%, and the tracking accuracy is 0.08°. Using the cosine law of illuminance, the error introduced by the incident angle is approximately 0.14%. On the test day, the weather was clear at noon, and the total measurement duration was less than 10 s, during which the variation in ground-based SSI was estimated at 0.1%. The uncertainty caused by atmospheric inhomogeneity was estimated to be 0.2%. In summary, the relative radiometric calibration accuracy across the entire spectral range was calculated to be 0.35%. A summary of the results is provided in Table 5.

The primary sources of spectral calibration uncertainty include the instrument's wavelength repeatability, the wavelength accuracy of the laser output, and the accuracy of the spectral calibration algorithm. The measurement repeatability of the instrument is evaluated based on wavelength repeatability. According to the factory spectral test report, the wavelength repeatability of GSSIM does not exceed 0.003 nm, and thus, a value of 0.003 nm is used for repeatability calculations. The Ekspla NT242 OPO laser's wavelength accuracy contributes a maximum error of 0.2 nm, and a range of 0–0.2 nm is used for uncertainty calculations. The uncertainty introduced by the spectral calibration algorithm is assessed

using wavelength accuracy. According to the fitted results from this test at 400.195 nm and 700.223 nm, the wavelength accuracy is taken as 0.195 nm to 0.223 nm in this calculation. Consequently, the overall spectral calibration uncertainty is calculated to be approximately 0.195 nm to 0.299 nm, as summarized in Table 6.

Table 5. Relative Radiometric Calibration Accuracy of GSSIM.

Source of Uncertainty		Uncertainty (%)	Combined Uncertainty (%)
GSSIM	Measurement Repeatability	0.226	
	solar tracking accuracy	0.14 (k = 1)	
Light Source (Solar)	Solar Radiation Instability	0.1	
Observation Environment	atmospheric inhomogeneity	0.2	
			0.347

Table 6. Spectral Calibration Accuracy of GSSIM.

Source of Uncertainty		Uncertainty (nm)	Combined Uncertainty (nm)
GSSIM	Wavelength Repeatability	0.003	
Light Source (Solar)	Wavelength Accuracy	0~0.2	
Spectral Calibration Algorithm	Wavelength Accuracy	0.195~0.223	
			0.195~0.299

The primary sources of absolute radiometric calibration uncertainty include the variability of the light source (spaceborne SSI), the atmospheric stability on calibration days, the instrument's observational uncertainties, and the uncertainties introduced by the calibration algorithm. Based on historical observation data from the FY-3E SSIM, the monthly variation in spaceborne SSI is estimated to be 0.5%. The uncertainty caused by atmospheric stability is assessed using the Langley plot correlation coefficient, with an average value of 0.31% across all wavelengths. Algorithm-related uncertainties include errors from Langley plot parameters (e.g., AM and R^2) and interpolation, which are estimated to contribute an uncertainty of 1%.

The instrument's observational uncertainty primarily arises from dark noise, spectral calibration accuracy, and the stability of the instrument's observations. When the instrument's DN values range from 1000 to 10,000, the uncertainty introduced by noise is approximately 0.010% to 0.089%. The spectral calibration uncertainty causes a spectral shift in the measured SSI, either left or right, by one spectral uncertainty. To evaluate this, the standard ground-based SSI spectrum was shifted accordingly, and interpolation was used to calculate the resulting SSI deviation. The relative SSI variation due to spectral shifts was found to range from 0.2% to 0.26%. The stability of the instrument's observations is represented by the relative radiometric calibration accuracy, with an uncertainty of 0.347%. The final calculated absolute radiometric calibration uncertainty ranges from 1.23% to 1.24%, as summarized in Table 7.

Table 7. Absolute Radiometric Calibration Accuracy of GSSIM.

Source of Uncertainty		Uncertainty (%)	Combined Uncertainty (%)
GSSIM	Noise	0.010~0.089 (k = 1.96)	
	Spectral Calibration Uncertainty	0.2~0.26	
	Relative Radiometric Calibration Accuracy	0.347	
Light Source (Solar)	Monthly Variation in Spaceborne SSI	0.5	
Observation Environment	atmospheric inhomogeneity	0.31	
Algorithm		1	
			1.23~1.24

4. Results and Discussion

4.1. SSI

We used the solar spectrum provided by ASTM G-173-03 as the standard reference. This spectrum is defined as the sum of the direct solar beam and the circumsolar component within a 2.5° disk around the Sun at an air mass of 1.5. The ASTM G-173-03 spectrum references direct SSI measurements from regions in the United States with latitudes similar to that of Lijiang, making it a suitable comparison for the Lijiang spectrum [32]. The comparisons between the two spectra in the 400–600 nm and 650–850 nm bands are shown in Figure 12a,b. The SSI at AM = 1.5 in Lijiang is 7.89% higher than ASTM G-173-03 in the 400–600 nm band, while in the 650–850 nm band, the difference is only 3.1%. This is attributed to Lijiang's lower latitude, higher altitude, and thinner atmosphere, which result in weaker extinction in the shortwave and visible bands. Consequently, Lijiang exhibits higher SSI in these bands but shows little difference in longer, non-absorptive bands. This result is consistent with the observations by Pudowan et al. in Ali and Shanghai [33].

Fraunhofer dark lines in the solar spectrum also provide opportunities for wavelength calibration. Figure 13a,b show the SSI measurements by GSSIM near two Fe dark lines: the e-line at 438.355 nm and the E_2-line at 527.039 nm. For comparison, the SSI from ASTM G-173-03 is also included. Molecular collisions in the atmosphere cause level perturbations that lead to the broadening of Fraunhofer dark lines, primarily exhibiting a Lorentzian line shape. Therefore, Lorentzian fitting was applied to the SSI measurement points to determine the central wavelengths of the dark lines. The fitting correlation coefficients (r) were all greater than 0.99. The wavelength accuracy for the Fe e-line and E_2-line was found to be 0.23 nm and 0.24 nm, respectively. Table 8 summarizes the results for other characteristic Fraunhofer dark lines. In the O_2 absorption band, the broader width and the inability of the instrument's spectral resolution to distinguish closely spaced dark lines resulted in larger wavelength deviations during Lorentzian fitting. However, the overall results indicate that the wavelength accuracy ($\delta\lambda$) is less than 0.3 nm, consistent with the results of the previous spectral tests. It is noteworthy that the SSI in Figure 12b exhibits wavelength-dependent fluctuations. We attribute this to interference between the mirror at the end of the instrument's optical tube and the fiber optic end face, which will be a focus of future work. In this section, we focused solely on verifying the wavelength calibration results.

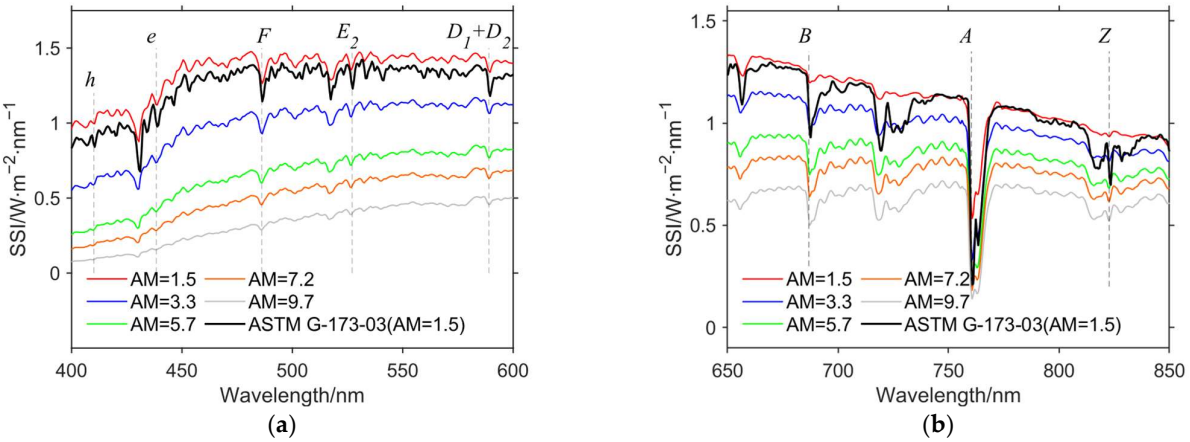


Figure 12. Langley plot-averaged solar spectrum for day 5 (AM = 1.5). (**a**) Solar spectrum with Fraunhofer lines in the 400–600 nm band; (**b**) Solar spectrum with Fraunhofer dark lines in the 650–850 nm band.

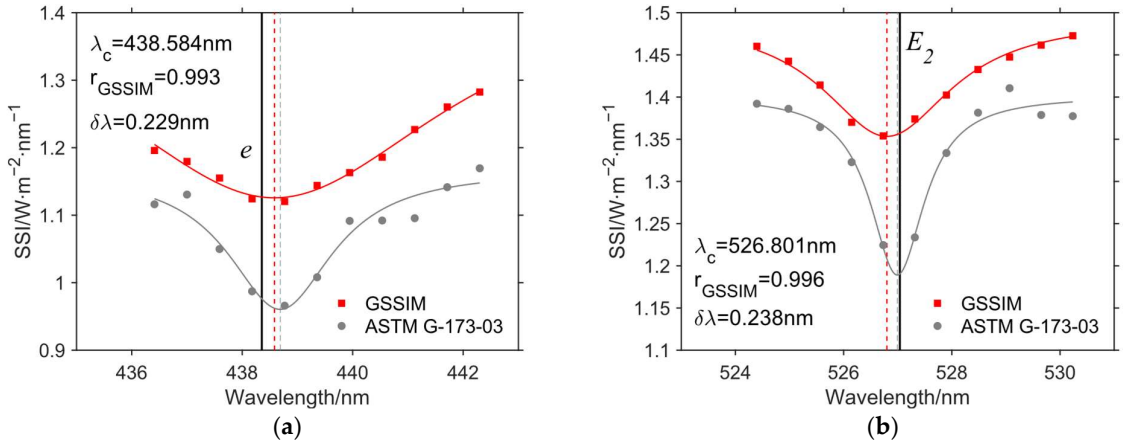


Figure 13. Atmospherically broadened Fraunhofer dark lines conforming to Lorentzian line shapes. (**a**) Fe e-line; (**b**) Fe E_2-line.

Table 8. Wavelength Testing Results of GSSIM for Selected Fraunhofer Dark Lines.

Name	Element	Wavelength (nm)	GSSIM Central Wavelength (nm)	δλ (nm)
h	H-δ	410.175	409.962	0.213
e	Fe	438.355	438.584	0.229
F	H-β	486.134	486.327	0.193
E_2	Fe	527.039	526.801	0.238
B	O2	686.719	688.097	1.378
A	O2	759.37	761.138	1.768
Z	O2	822.696	822.866	0.17

4.2. AOD

Using the AOD data observed by CE318 in the Lijiang region as a reference, we evaluated the accuracy of the Langley plot calibration results by comparing the daily averaged AOD from GSSIM on day 1 with CE318. The total atmospheric optical depth (τ_{total}) calculated using the Langley plot is considered to be the sum of the Rayleigh scattering contribution ($\tau_{Rayleigh}$), the optical depth due to absorption cross-sections, and the aerosol optical depth (AOD). The Rayleigh scattering for the calibration day was computed based on the atmospheric pressure and altitude of the Lijiang region [34]. Figure 14a,b

show the aerosol optical depth ($\tau_{total} - \tau_{Rayleigh}$) derived from the averaged Langley plot and the integrated Langley plot, represented by black solid lines. In absorption bands such as O_3 (Chappuis), O_2 (760 nm), and H_2O (936 nm), an increase in optical depth is observed, which aligns with the absorption cross-section of these gases. The mean relative deviations of AOD between the two Langley plot methods and CE318 are 3.2% in non-gas absorption bands and 2.1% in gas absorption bands. These results are consistent with the conclusions about the responsivity deviations of 0.78% and 0.51% derived in Figure 11b, indicating that responsivity deviations propagate and amplify into the AOD retrieval. In non-gas absorption bands, the reduced measurement repeatability and lower signal-to-noise ratio (SNR) at the CCD's spectral range edges result in larger optical depth inversion deviations for both methods. By subtracting the theoretical Rayleigh scattering optical depth from the total optical depth derived using the Langley plot, a low-order polynomial fit is applied to the results at non-gas absorption bands, such as 440 nm and 870 nm, to obtain the wavelength dependence of AOD [35], as indicated by the red dashed lines in Figure 14a,b. Additionally, the green squares represent the daily averaged AOD measured by CE318 at seven wavelengths, demonstrating consistency between the AOD retrieval results of CE318 and GSSIM.

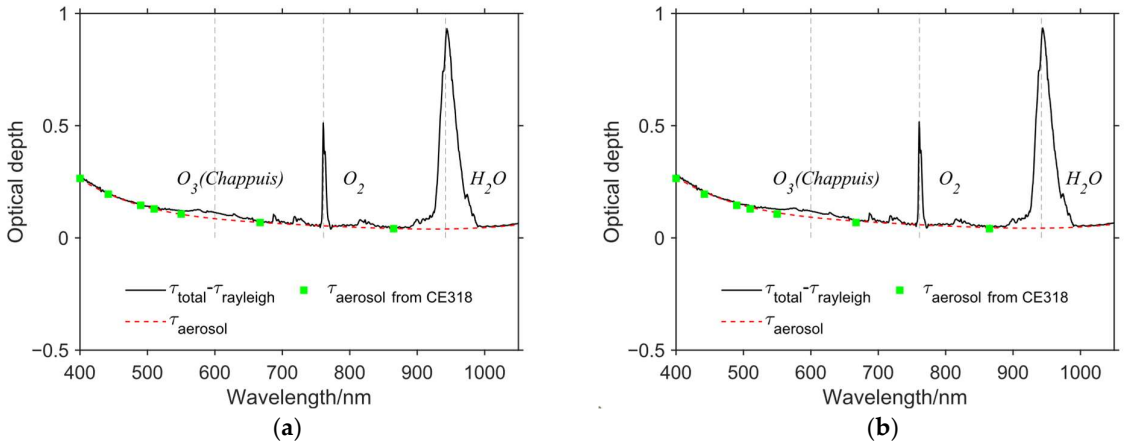


Figure 14. Comparison of AOD retrieved by GSSIM using two Langley plot calibration methods with CE318 retrievals. (**a**) Averaged Langley plot method; (**b**) Integrated Langley plot method.

Figure 15 presents the absolute deviations of AOD at the seven non-gas absorption wavelengths. The mean absolute AOD deviations at the seven wavelengths are 0.0056 for the averaged Langley plot method and 0.0046 for the integrated Langley plot method. Moreover, the coefficient of variation (CV) of absolute deviations across wavelengths is smaller for the integrated Langley plot method. This indicates that, based on the criterion of absolute AOD deviation, the integrated Langley plot method is more suitable for radiometric field calibration in Lijiang during March. It should be noted that these results benefit from the high altitude and clean atmosphere of Lijiang, where the integration of calibration day data did not introduce significant bias in spectral responsivity. Further validation of this method's reliability is required in areas with different conditions, such as urban aerosols and other types of environments.

To further validate the results, a correlation analysis was conducted between the AOD observations from CE318 and GSSIM. The scatter plots in Figures 16 and 17 illustrate the correlation between AOD retrieved by the two Langley plot methods and the standard instrument. The color of the scatter plot points represents the spectrometer's temperature, which influences the spectral responsivity of the entire GSSIM radiometric calibration. The AOD retrieval results from GSSIM and CE318 exhibit excellent consistency across all wavelengths, with correlation coefficients exceeding 0.94. The AOD retrieved using

the integrated Langley plot method is closer to the true values, although the correlation coefficient r is only improved by 0.9–2.7% compared to the averaged Langley plot method. The integrated Langley plot method also exhibits a smaller RMSE in the linear fit with the true values, with slopes ranging from 0.97 to 0.99. The low slope is attributed to the relative underestimation of SSI measurements at high optical depths and the relative overestimation at low optical depths. These deviations are likely caused by differences in the positioning of the two instruments, dark noise, and measurement repeatability. In GSSIM, although a temperature control unit is included, the spectrometer's temperature still exhibits periodic variations of several degrees Celsius. While the temperature control mitigates wavelength drift, as shown in Figure 12a,b, further correction of the instrument's spectral responsivity to temperature sensitivity remains necessary. This correction aims to quantify the radiometric calibration uncertainty induced by actual temperature fluctuations, thereby enhancing the accuracy of AOD retrieval.

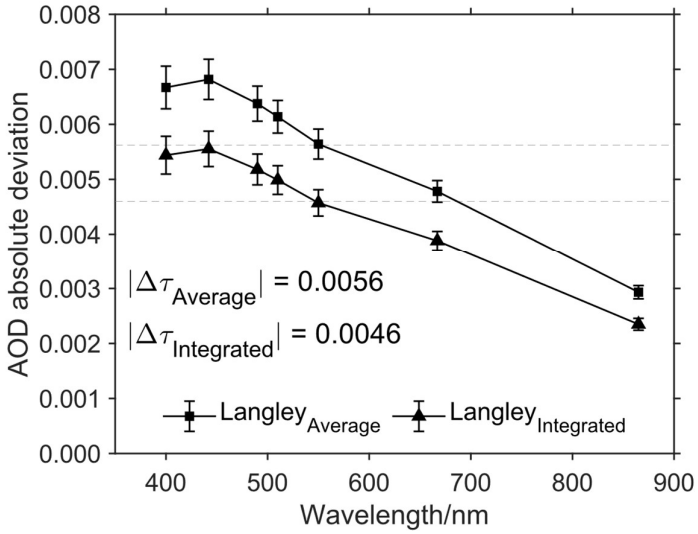


Figure 15. Absolute Deviations Between AOD Retrieved by Two Langley Plot Calibration Methods and CE318 Observations.

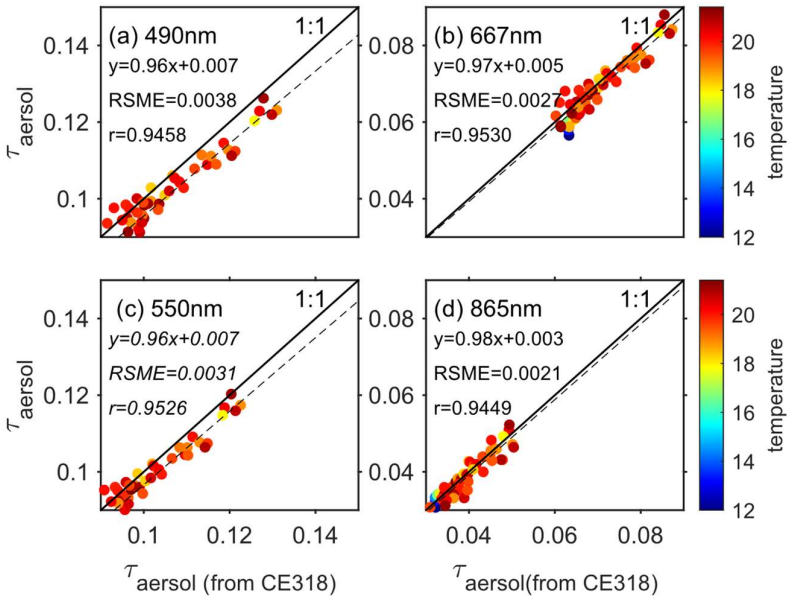


Figure 16. Linear Correlation Between AOD Retrieved by the Averaged Langley Plot Method and AOD Measured by the Standard Instrument.

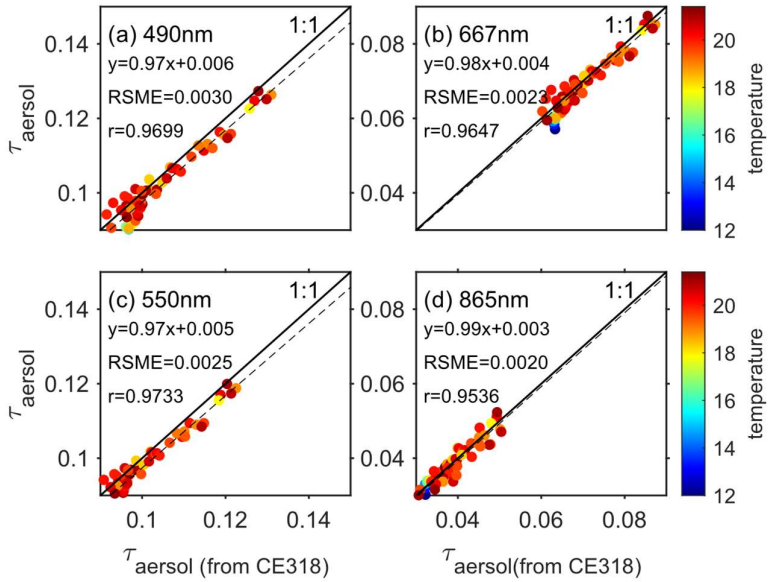


Figure 17. Linear Correlation Between AOD Retrieved by the Integrated Langley Plot Method and AOD Measured by the Standard Instrument.

5. Conclusions

The spectral and radiometric calibration accuracy of SSI observation instruments determines the retrieval accuracy of atmospheric characteristics such as SSI and AOD. During field observations, environmental temperature variations affect the instrument's dark noise and calibration precision. To address this issue, a temperature control module was integrated into the observation instrument, and a pixel-level dynamic dark noise deduction method was implemented. This effectively suppressed and stabilized the dark noise throughout the day, with noise levels maintained at 0 ± 0.89 (k95 = 1.96), representing a 0.6% improvement over noise correction methods using temperature as the independent variable. Spectral testing with an OPO laser demonstrated a spectral accuracy of 0.23 nm, and the spectral calibration uncertainty of the instrument was assessed to be 0.195 nm to 0.299 nm. Comparisons with the standard solar spectrum and validations using Fraunhofer dark lines confirmed a wavelength accuracy of $\delta\lambda < 0.3$ nm. Using the Sun as the light source for short-duration measurements, the instrument exhibited a measurement repeatability of 0.226% in non-gas absorption bands. The relative radiometric calibration uncertainty was calculated to be 0.35%, demonstrating the instrument's high stability. Using March observation data from Lijiang, five days were selected as calibration days. The integrated Langley plot used in this study treats the five calibration days as a single dataset, which is more in line with the essence of the Langley plot. The results are then compared with those obtained using the averaged Langley plot. The spectral responsivity curves of the two methods differed by 0.80%, indicating consistency. In terms of AOD retrieval results, the integrated Langley plot method exhibited smaller absolute and relative deviations across seven bands and showed a higher linear correlation with CE318 measurements (r improved by 0.9~2.7%, RMSE = 0.002~0.003). The absolute radiometric calibration uncertainty of the integrated Langley plot method was estimated to be 1.23~1.24%.

The dynamic dark noise deduction method proposed in this study is well-suited for addressing noise variation issues in similar spectrometers and demonstrates the feasibility of using Fraunhofer dark lines for wavelength testing and calibration in ground-based SSI observation instruments. Additionally, the integrated Langley plot method is recommended as one of the radiometric calibration methods for springtime field campaigns in the Lijiang region.

Author Contributions: Conceptualization, methodology, validation, and writing—original draft preparation, G.L.; investigation, resources, A.Z.; funding acquisition, project administration, and data curation, Y.H.; formal analysis and writing—review and editing, Z.L.; supervision and visualization, X.Y. All authors have read and agreed to the published version of the manuscript.

Funding: This research received no external funding.

Data Availability Statement: The project is currently in the pilot operation and construction phase, and the data are not publicly available due to secrecy.

Conflicts of Interest: The authors declare no conflicts of interest.

References

1. Brown, H.; Liu, X.; Feng, Y.; Jiang, Y.; Wu, M.; Lu, Z.; Wu, C.; Murphy, S.; Pokhrel, R. Radiative effect and climate impacts of brown carbon with the Community Atmosphere Model (CAM5). *Atmos. Chem. Phys.* **2018**, *18*, 17745–17768. [CrossRef]
2. Charlesworth, E.; Plöger, F.; Birner, T.; Baikhadzhaev, R.; Abalos, M.; Abraham, N.L.; Akiyoshi, H.; Bekki, S.; Dennison, F.; Jöckel, P.; et al. Stratospheric water vapor affecting atmospheric circulation. *Nat. Commun.* **2023**, *14*, 3925. [CrossRef] [PubMed]
3. Poulsen, C.J.; Tabor, C.; White, J.D. Long-term climate forcing by atmospheric oxygen concentrations. *Science* **2015**, *348*, 1238–1241. [CrossRef] [PubMed]
4. Levy, H., II; Horowitz, L.W.; Schwarzkopf, M.D.; Ming, Y.; Golaz, J.; Naik, V.; Ramaswamy, V. The roles of aerosol direct and indirect effects in past and future climate change. *J. Geophys. Res.-Atmos.* **2013**, *118*, 4521–4532. [CrossRef]
5. Wang, J.; Li, J.; Ye, J.; Zhao, J.; Wu, Y.; Hu, J.; Liu, D.; Nie, D.; Shen, F.; Huang, X.; et al. Fast sulfate formation from oxidation of SO_2 by NO_2 and HONO observed in Beijing haze. *Nat. Commun.* **2020**, *11*, 2844. [CrossRef] [PubMed]
6. Zhang, S.; Wu, J.; Fan, W.; Yang, Q.; Zhao, D. Review of aerosol optical depth retrieval using visibility data. *Earth-Sci. Rev.* **2020**, *200*, 102986. [CrossRef]
7. Zhang, X.Y.; Wang, Y.Q.; Zhang, X.C.; Guo, W.; Niu, T.; Gong, S.L.; Yin, Y.; Zhao, P.; Jin, J.L.; Yu, M. Aerosol monitoring at multiple locations in China: Contributions of EC and dust to aerosol light absorption. *Tellus Ser. B-Chem. Phys. Meteorol.* **2008**, *60*, 647–656. [CrossRef]
8. Lim, S.S.; Vos, T.; Flaxman, A.D.; Danaei, G.; Shibuya, K.; Adair-Rohani, H.; AlMazroa, M.A.; Amann, M.; Anderson, H.R.; Andrews, K.G.; et al. A comparative risk assessment of burden of disease and injury attributable to 67 risk factors and risk factor clusters in 21 regions, 1990–2010: A systematic analysis for the Global Burden of Disease Study 2010. *Lancet* **2012**, *380*, 2224–2260. [CrossRef]
9. Sokolik, I.N.; Toon, O.B. Direct radiative forcing by anthropogenic airborne mineral aerosols. *Nature* **1996**, *381*, 681–683. [CrossRef]
10. Zhang, H.; Zhao, S.Y.; Wang, Z.L.; Zhang, X.Y.; Song, L.C. The updated effective radiative forcing of major anthropogenic aerosols and their effects on global climate at present and in the future. *Int. J. Climatol.* **2016**, *36*, 4029–4044. [CrossRef]
11. Kramer, R.J.; He, H.; Soden, B.J.; Oreopoulos, L.; Myhre, G.; Forster, P.M.; Smith, C.J. Observational Evidence of Increasing Global Radiative Forcing. *Geophys. Res. Lett.* **2021**, *48*, e2020GL091585. [CrossRef]
12. Dergiades, T.; Kaufmann, R.K.; Panagiotidis, T. Long-run changes in radiative forcing and surface temperature: The effect of human activity over the last five centuries. *J. Environ. Econ. Manag.* **2016**, *76*, 67–85. [CrossRef]
13. Nakajima, T.; Sekiguchi, M.; Takemura, T.; Uno, I.; Higurashi, A.; Kim, D.; Sohn, B.J.; Oh, S.-N.; Nakajima, T.Y.; Ohta, S.; et al. Significance of direct and indirect radiative forcings of aerosols in the East China Sea region. *J. Geophys. Res. Atmos.* **2003**, *108*, 8658. [CrossRef]
14. Vitale, D.; Bilancia, M. Role of the natural and anthropogenic radiative forcings on global warming: Evidence from cointegration-VECM analysis. *Environ. Ecol. Stat.* **2013**, *20*, 413–444. [CrossRef]
15. Che, H.; Xia, X.; Zhu, J.; Wang, H.; Wang, Y.; Sun, J.; Zhang, X.; Shi, G. Aerosol optical properties under the condition of heavy haze over an urban site of Beijing, China. *Environ. Sci. Pollut. Res.* **2015**, *22*, 1043–1053. [CrossRef] [PubMed]
16. Zhao, H.; Che, H.; Zhang, X.; Ma, Y.; Wang, Y.; Wang, X.; Liu, C.; Hou, B.; Che, H. Aerosol optical properties over urban and industrial region of Northeast China by using ground-based sun-photometer measurement. *Atmos. Environ.* **2013**, *75*, 270–278. [CrossRef]
17. Pan, L.; Che, H.; Geng, F.; Xia, X.; Wang, Y.; Zhu, C.; Chen, M.; Gao, W.; Guo, J. Aerosol optical properties based on ground measurements over the Chinese Yangtze Delta Region. *Atmos. Environ.* **2010**, *44*, 2587–2596. [CrossRef]
18. Che, H.; Wang, Y.; Sun, J. Aerosol optical properties at Mt. Waliguan Observatory, China. *Atmos. Environ.* **2011**, *45*, 6004–6009. [CrossRef]
19. Ogunjobi, K.; He, Z.; Simmer, C. Spectral aerosol optical properties from AERONET Sun-photometric measurements over West Africa. *Atmos. Res.* **2008**, *88*, 89–107. [CrossRef]

20. Zhang, M.; Gong, W.; Ma, Y.; Wang, L.; Chen, Z. Transmission and division of total optical depth method: A universal calibration method for Sun photometric measurements. *Geophys. Res. Lett.* **2016**, *43*, 2974–2980. [CrossRef]
21. Xu, Q.; Zheng, X.; Li, Z.; Zhang, W.; Wang, X.; Li, J.; Li, X. Absolute spectral radiance responsivity calibration of sun photometers. *Rev. Sci. Instrum.* **2010**, *81*, 033103. [CrossRef] [PubMed]
22. Redondas, A.; Nevas, S.; Berjón, A.; Sildoja, M.-M.; León-Luis, S.F.; Carreño, V.; Santana-Díaz, D. Wavelength calibration of Brewer spectrophotometer using a tunable pulsed laser and implications to the Brewer ozone retrieval. *Atmos. Meas. Tech.* **2018**, *11*, 3759–3768. [CrossRef]
23. Guo, Y.; Gong, C.; Hu, Y.; Zheng, F.; Liu, Y. On-Orbit Wavelength Calibration Error Analysis of the Spaceborne Hyperspectral Greenhouse Gas Monitoring Instrument Using the Solar Fraunhofer Lines. *Remote Sens.* **2024**, *16*, 3367. [CrossRef]
24. Zhai, W.; Li, J.; Zheng, X.; Li, Z.; Meng, B.; Zhang, W.; Wang, X. Research on Method of Calibrating Sun Channels of Sun Radiometers. *Acta Opt. Sin.* **2012**, *32*, 131–136.
25. Bolsée, D.; Pereira, N.; Decuyper, W.; Gillotay, D.; Yu, H.; Sperfeld, P.; Pape, S.; Cuevas, E.; Redondas, A.; Hernandéz, Y.; et al. Accurate Determination of the TOA Solar Spectral NIR Irradiance Using a Primary Standard Source and the Bouguer-Langley Technique. *Sol. Phys.* **2014**, *289*, 2433–2457. [CrossRef]
26. Toledano, C.; González, R.; Fuertes, D.; Cuevas, E.; Eck, T.F.; Kazadzis, S.; Kouremeti, N.; Gröbner, J.; Goloub, P.; Blarel, L.; et al. Assessment of Sun photometer Langley calibration at the high-elevation sites Mauna Loa and Izana. *Atmos. Chem. Phys.* **2018**, *18*, 14555–14567. [CrossRef]
27. Kouremeti, N.; Nevas, S.; Kazadzis, S.; Gröbner, J.; Schneider, P.; Schwind, K.M. SI-traceable solar irradiance measurements for aerosol optical depth retrieval. *Metrologia* **2022**, *59*, 044001. [CrossRef]
28. Li, J.Y.; Wei, H.L.; Xu, Q.S.; Zhan, J. Atmospheric aerosol optical characteristics measured at several typical zones in China. *Opt. Precis. Eng.* **2012**, *20*, 1166–1174.
29. Estellés, V.; Campanelli, M.; Smyth, T.J.; Utrillas, M.P.; Martínez-Lozano, J.A. AERONET and Euroskyrad (ESR) aerosol optical depth intercomparison on Cimel CE318 and Prede POM01 radiometers. In Proceedings of the Conference on Remote Sensing of Clouds and the Atmosphere XV, Toulouse, France, 21–23 September 2010; p. 78270Y.
30. Tang, X.X.; Li, J.-Y.; Xu, G.; Sun, F.-Y.; Dai, C.-M.; Wei, H.-L. Mixing Calibration Method for Spectral Sun-Photometer. *Spectrosc. Spectr. Anal.* **2023**, *43*, 2536–2542.
31. Stubbs, C.W.; Doherty, P.; Cramer, C.; Narayan, G.; Brown, Y.J.; Lykke, K.R.; Woodward, J.T.; Tonry, J.L. Precise Throughput Determination of the Panstarrs Telescope and the Gigapixel Imager Using a Calibrated Silicon Photodiode and a Tunable Laser: Initial Results. *Astrophys. J. Suppl. Ser.* **2010**, *191*, 376–388. [CrossRef]
32. Soria-Moya, A.; Fernández, E.F.; Almonacid, F.; Mallick, T.K. Spectral losses of high concentrator photovoltaic modules depending on latitude. *AIP Conf. Proc.* **2015**, *1679*, 050013.
33. Pu, D.W.; Lagba, T.; Sheng, M.; Liu, J.; Wang, Q.; Wang, M.-M.; Zhou, Y.; Lu, H.-Y.; Tsoja, W.; Norsang, G. Surface Solar Spectral Observation Along 30° N in China. *Spectrosc. Spectr. Anal.* **2023**, *43*, 1881–1887.
34. Hansen, J.E.; Travis, L.D. Light-Scattering in Planetary Atmospheres. *Space Sci. Rev.* **1974**, *16*, 527–610. [CrossRef]
35. Jeong, U.; Tsay, S.; Pantina, P.; Butler, J.J.; Loftus, A.M.; Abuhassan, N.; Herman, J.R.; Dimov, A.; Holben, B.N.; Swap, R.J. Langley Calibration Analysis of Solar Spectroradiometric Measurements: Spectral Aerosol Optical Thickness Retrievals. *J. Geophys. Res. Atmos.* **2018**, *123*, 4221–4238. [CrossRef]

Disclaimer/Publisher's Note: The statements, opinions and data contained in all publications are solely those of the individual author(s) and contributor(s) and not of MDPI and/or the editor(s). MDPI and/or the editor(s) disclaim responsibility for any injury to people or property resulting from any ideas, methods, instructions or products referred to in the content.